Characterization of Particle Coalescence in Waterborne Coatings Using Atomic Force Microscopy

R.M. Rynders, C.R. Hegedus, and A.G. Gilicinski—Air Products and Chemicals, Inc.*

Atomic force microscopy (AFM) was used to image coatings formed from blends containing various ratios of three waterborne acrylic/polyurethane hybrid polymers. Tapping and contact mode AFM were evaluated for this application, and tapping mode proved to be the best method due to the low friction forces. It was shown that when the tip and feature sizes were similar, the superposition of the tip morphology on the surface features in the AFM image was significant. AFM imaging of gold colloids dispersed on mica and scanning electron microscopy of the tip were used to characterize the AFM tips. A method was developed to estimate the tip radii; in turn, the tip size was accounted for in analyzing the dimensions of the coating surface features. The degree of particle coalescence was evaluated from the AFM images. The polymer blends were ranked according to the degree of particle coalescence; and the results correlated well with other methods of characterization.

INTRODUCTION

The technical objectives of this effort were: (1) to develop a methodology using atomic force microscopy (AFM) to examine coating/paint surface morphologies; and (2) to apply this technique in the quantitative assessment of waterborne latex film formation. The latter objective was approached by analyzing coatings formed from blends of latex particles which varied in hardness, thus displaying a wide range of film formation potential.

Coating Performance Issues

The interest in waterborne polymeric coatings is growing tremendously due to environmental protection and worker safety concerns. Aqueous systems offer the potential to significantly reduce emissions of volatile organic compounds (VOCs) compared to their solvent-borne counterparts. Use of waterborne coatings has been well-established in low to moderate duty applications such as architectural coatings, wood finishes, floor polishes, printing inks, and business machine coatings. Advances in polymer synthesis and coating formulation technologies are increasing the potential for use of polymeric materials in higher performance, heavy duty applications.

Traditional waterborne coatings are prepared from an aqueous dispersion of polymer particles, commonly referred to as a latex. Other ingredients within the coating may include pigments, solvents, and additives (i.e., surfactants, rheology modifiers, adhesion promoters, etc.). The ultimate performance of the applied coating is highly dependent on the quality of the film, which is formed by coalescence of latex particles as volatile components evaporate. Some latex coatings coalesce well and produce continuous, nonporous films. Other coatings coalesce poorly and produce films with cracks, high porosity, or even a powdery residue. In some cases, defects from poor film formation are microscopic and difficult to ascertain; nonetheless, they adversely affect strength, flexibility, protection of the substrate, and other critical coating properties.

Figure 1 is a schematic that depicts the generally accepted mechanism for film formation. Upon application of the latex, water and other volatile components begin to evaporate, forcing the polymer particles closer together to form a solid film on the substrate. Numerous models and mechanisms have been proposed to describe formation of films from latex dispersions. Dillon et al.[1] proposed that as water and other volatiles evaporate, neighboring latex particles are forced into intimate contact due to surface tension of the polymer. The process is followed by dry sintering (dry caking); coalescence of the particles occurs by viscous flow. Brown[2] suggested that both particle-particle attraction and repulsive forces exist from a number of sources, including interstitial capillary forces, van der Waals forces between spheres, coulombic repulsion, and resistance to deformation. Each of these forces can be measured or calculated for specific latex systems. Coalescence

Presented at the 72nd Annual Meeting of the Federation of Societies for Coatings Technology, October 13, 1994, New Orleans, LA.

*7201 Hamilton Blvd., Allentown, PA 18195-1501.

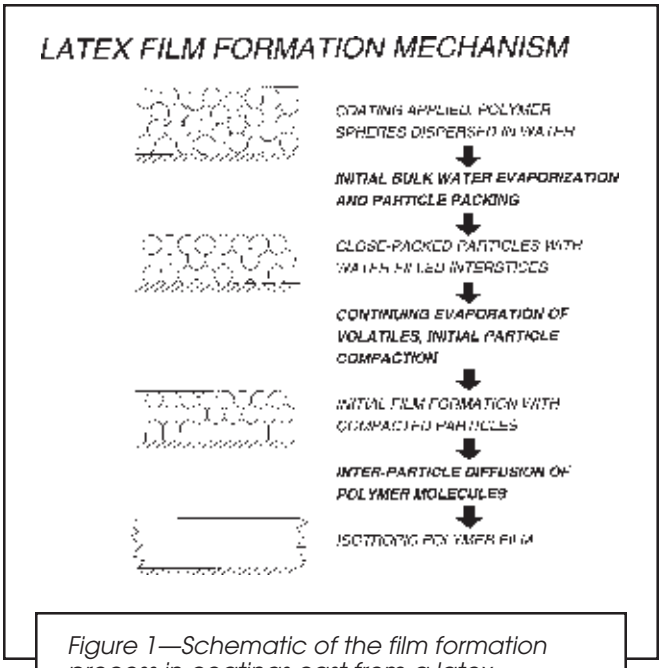

Figure 1—Schematic of the film formation process in coatings cast from a latex.

occurs when the attractive forces between particles are higher than the repulsive forces. Vanderhoff[3] proposed that as particles approach each other, their electrical double layers hinder intimate contact. Additional water evaporation exerts a force due to the surface tension which can rupture adjacent double layers, causing polymer-polymer contact (wet caking). The remaining polymer/water surface tension then increases the particle-particle contact pressure, causing further coalescence. Sheets et al.[4] suggested that capillary forces cause initial film formation (similar to Brown). After close particle packing, further coalescence is controlled by complete diffusion of water out of the coating. Voyutskii et al.[5] theorized that the critical contributions to film formation occur during the latter stages of coalescence when polymer chains diffuse from particle to particle. The residual structure of spherical particles diminishes and the film becomes homogenous and cohesive. This process is commonly referred to as autohesion or self-diffusion. Eckersley et al.[6] proposed that as water evaporates, both interfacial and capillary forces in the water-filled interstices of the particles cause viscoelastic behavior in the polymer. This response results in particle-particle contact and eventual film coalescence.

Although the suggested mechanisms of film formation differ, most agree that good film formation requires diffusion of polymer molecules from particle to particle as the coating dries and adjacent particles come into contact. As this diffusion occurs, coalescence becomes complete and cohesive strength of the film is enhanced significantly by increased chain entanglements and secondary bonding. The diffusion process is associated with the onset of large-scale motion of molecular chains, such that polymers at temperatures above their glass transition temperature (T_g), will form films more easily than those below their T_g or with high molecular weights. Unfortunately, polymers with lower T_gs normally produce coatings with lower strength, durability, and chemical resistance. These properties are required for many high performance applications.

The balance that must be attained between film formation and mechanical properties of the coating is exemplified in a series of aqueous acrylic-polyurethane hybrid dispersions.* These materials are latex dispersions containing acrylic and polyurethane chains that are entangled at the molecular level. This molecular level mixing significantly improves the mechanical and chemical resistance properties compared to coatings prepared from traditional, physically blended materials. Pertaining to the film, two of the hybrids, Flexthane 610 and 620, will film form at room temperature (T_g range is –40 to 50°C), but the films are relatively soft. In contrast, the film formed by Flexthane 630 is harder (T_g range exceeds 100°C), but it will not adequately film form at room temperature without added co-solvents. It would be desirable to have a dispersion with the film formation properties of 610 and 620, while exhibiting the hardness of 630.

The traditional approach to achieving these improved performance characteristics is to use harder polymers with high glass transition temperatures and add organic solvents, surfactants, and/or other plasticizers to the latex. These added ingredients improve coalescence by swelling (softening) the polymer and lowering the T_g of the system. Unfortunately, these ingredients also have the undesired side effect of increasing the VOCs of the emulsions, which negates one of the main advantages of water-based systems. Also, the additives may have a detrimental effect on the water resistance of the applied coating.

An alternative approach to improve film formation without added coalescing aids is to mix dispersions of soft (low T_g) and hard (high T_g) polymers. In this manner, the soft particles may coalesce around the harder particles to produce a composite-like effect. Preliminary studies performed with various mixtures of 610, 620, and 630 suggested that some mixtures had the potential to form high quality, continuous films that were relatively hard, tough, and durable. Although promising synergistic coating properties were observed with some of these mixtures, other mixtures displayed less attractive properties due to the apparent tradeoff between hardness and good film formation. A problem encountered in these preliminary studies was the lack of a method to accurately assess film formation characteristics, i.e., extent of particle coalescence. This assessment was necessary in order to define the effects of film formation on coating properties and to determine the potential for long-term performance properties of applied coating systems.

Coating film formation is difficult to study, and it is especially difficult to quantify the degree of particle coalescence. Analytical techniques applied to studies of film formation include scanning electron microscopy (SEM),[3,6-8] small angle neutron scattering (SANS),[9-11] and nonradiative energy transfer techniques.[12] More conventionally, the extent of particle coalescence and quality of film formation have been deduced from mechanical properties of polymer films.[6] The results generated from such methods do not provide explicit, quantitative data that describe the extent of particle coalescence. Of these methods, SEM provides the most direct information on film morphology. However, with small particle size latexes, such as the 40-60 nm particle sizes of these hybrid polymers, the three-dimensional aspects of the surface features are difficult to ascertain by SEM.

*Flexthane® 610, 620, and 630, Air Products and Chemicals, Inc.

Concerning a closely related issue, ASTM D 2354 describes a method to determine minimum film formation temperature (MFFT) of emulsion (including latex) coatings. The procedure is performed by using an instrument consisting of a substrate plate with a temperature gradient. The coating is cast on the plate and allowed to dry at the substrate temperature. After the film has dried, it is visually inspected for film formation damage, such as cracks and other discontinuities. The lowest temperature on the substrate at which a consistent and coherent film is formed is the MFFT. This test is more simplistic than those described previously, although it is extremely practical for quick evaluations. It allows for the determination of the MFFT at a visual (or slightly magnified) level; however, it provides little insight into the details of particle coalescence, film formation, or film quality.

Atomic force microscopy (AFM) has recently emerged as a tool that can produce three-dimensional results of surface morphologies on a 10^{-10} to 10^{-6} meter scale.[13,14] AFM is, therefore, an ideal technique to study coating morphologies. In addition to enhanced resolution, the AFM offers distinct advantages over the SEM. A key advantage of AFM lies with the ease of sample preparation and the ability to examine nonconductive surfaces in ambient conditions or under fluid. In addition, AFM provides three-dimensional numerical data that can be analyzed quantitatively using image analysis software. If our hypothesis that coating morphology reflects the extent of particle coalescence is correct, the AFM can provide direct, quantitative information on the film formation quality.

AFM Imaging Issues

AFM has been used to study film formation of polymeric materials.[15-19] As with any technique, artifacts associated with AFM can lead to misinterpretation of the results. Since soft materials, such as polymers, were first imaged, it was recognized that sample deformation could be a problem under forces that are present during the imaging process (van der Waals, capillary, friction, and electrostatic forces).[20] Contact mode AFM (CMAFM) was the original mode in which AFM was implemented in 1986. In this mode, the surface is scanned beneath a stationary tip. Frictional forces between the sample and the tip can be sufficiently high to damage a soft surface. To reduce frictional forces imposed on the surface by this scanning mechanism, a method known as tapping mode AFM (TMAFM) was invented in 1992. In tapping mode AFM, the sample is scanned beneath a tip that is attached to a bimorph driver that oscillates the cantilever at frequencies in the range of 300 kHz, which is two orders of magnitude greater than the scanning frequency. In this manner, the same information obtained from CMAFM is collected without the frictional forces imposed by CMAFM.

A second caveat of AFM arises from artifacts induced by superposition of the AFM tip morphology on true surface features; careful interpretation is critical when features of interest are similar in size or smaller than the AFM tip radius.[21] Juhué et al.[18,19] have used AFM to study the effect of surfactants and annealing on poly(butyl methacrylate) latex film formation. The latex particle size was 300 nm, and they did not account for the 10% error introduced on the particle size by superposition of a 20-30 nm AFM tip radius. The particle size distribution of the hybrid polymer series investigated in this work ranged from 40-60 nm, and the tip size and morphology could not be ignored. Various methods for measuring the tip size and/or shape include reversal imaging (surface features of known size and shape are used to image the AFM tip),[22-26] height standard calibrations (calibration of AFM height data using a well-characterized stepped surface),[27,28] and force calculations.[29-31]

In this work, coatings formed from various blends of Flexthane 610, 620, and 630, were analyzed by AFM and the degree of particle coalescence of each film was assessed. Both contact and tapping mode AFM and three types of probe tips were used to determine the best method for imaging the films. The AFM results were compared to SEM micrographs of platinum-coated films. To account for the tip size and shape, reversal imaging was applied using gold colloids fixed to mica. The results from the AFM analyses were correlated with coating performance data from electrochemical impedance spectroscopy (EIS) and Prohesion™ tests. The results of this study were used to correlate the extent of film formation with coating performance and, more specifically, to select mixtures of 610, 620, and 630 that will provide optimal performance in waterborne coating formulations.

EXPERIMENTAL

Coating Sample Preparation

Commercially available samples of acrylic polyurethane hybrid dispersions (Flexthane 610, 620, and 630) were used in this evaluation. Their preparation and properties are described elsewhere.[32,33] The initial screening experiments for mixtures of the three dispersions were established according to a simplex centroid design[34] as listed in *Table* 1. Prior characterizations indicated a compositional region of improved coating properties and this area was highlighted and studied according to an extreme vertices mixture design.[35] These latter mixtures also are included in *Table* 1 and all of the coatings evaluated are illustrated on the tri-coordinate graph in *Figure* 2.

The coatings were prepared by mixing under mild agitation with a low speed mechanical stirrer for 10 to 15 min. The mixed coatings were allowed to sit for 24 hr before application

Table 1—Design Composition for Hybrid Mixtures

Sample ID	% Composition by Weight		
	610	620	630
Initial Simplex Design:			
A	100	0	0
B	50	50	0
C	0	100	0
D	0	50	50
E	0	0	100
F	50	0	50
G	66.6	16.7	16.7
H	16.7	66.6	16.7
I	16.7	16.7	66.6
J	33.3	33.3	33.3
Extreme Vertices Design:			
K	31	22	47
L	24	30	46
M	19	28	53
N	26	19	55

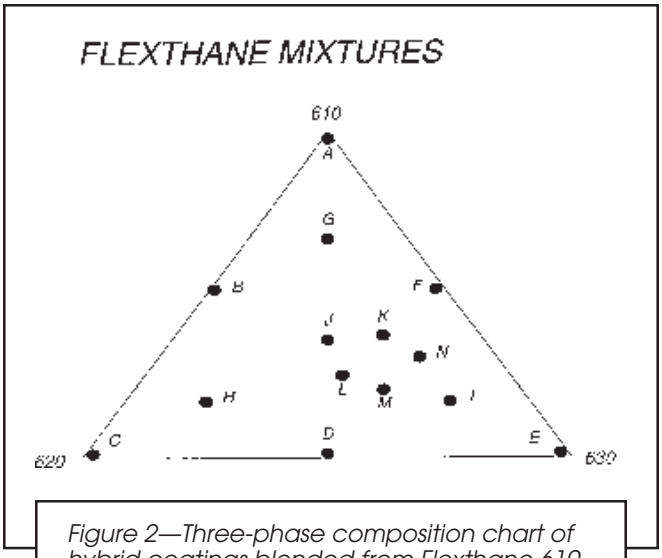

Figure 2—Three-phase composition chart of hybrid coatings blended from Flexthane 610, 620, and 630.

to steel specimens using a 152 micron (6 mil) draw-down bar. The metal substrates were cold-rolled 1020 steel with a zinc phosphate treatment (Bonderite 952). The substrate was measured to have an average roughness (Ra) of 1.5 microns. The applied coatings were cured at constant temperature and humidity conditions of 21°C and 50% relative humidity for 14 days prior to characterization. The dry film thickness was measured with a film thickness gauge to be 50.8 ± 7.6 microns.

Atomic Force Microscopy

Figure 3 is a schematic that shows the AFM imaging mechanism. In contact mode AFM, a sample surface is rastered in a plane perpendicular to a sharp tip held near the sample surface. As the forces on tip change, due to protruding or recessed features on the sample surface, the tip is deflected upward or downward, respectively. Concurrently, a laser beam signal is focused on the end of a cantilever that holds the tip. The deflection of the tip is then detected at a split photodiode by a change in position of the reflected laser beam. In tapping mode AFM, the scanning mechanism is as described previously, but the tip is oscillated at a frequency that is much higher than the sample horizontal scanning frequency. This "tapping" of the tip reduces frictional forces that are encountered in conventional contact made AFM.

A digital instruments nanoscope III multimode AFM using version 2.4 of the software and a 15 μm scanner head was used in both tapping and contact modes to image the coatings at a scan rate of 5 Hz. Images were collected at 1, 2, and 5 μm on three different regions of the surface.

A Pelco™ gold colloidal standard kit (Ted Pella) was used to disperse a mixture of gold colloid spheres on mica. The colloid diameters were certified by the manufacture to be 7.70 nm ± 7.74%, 14.36 nm ± 5.68%, and 27.80 nm ± 8.87%. Before each coating sample was imaged, the tip size and shape was checked with the gold standard. If the spherical shape of the colloids was distorted, the tip was not used. The analysis used to characterize the tips using the gold standards is described in detail in the Results and Discussion Section.

Scanning Electron Microscopy

The coated samples were glued to aluminum SEM sample mounts using conductive carbon paint and allowed to dry. An ion beam sputter coater (VCR Group, Inc. model TM 200S) was used to apply a 1 nm thick platinum film to enhance conductivity and signal for SEM.

SEM analysis was performed using a JEOL JSM-6300F field-emission scanning electron microscope. Secondary electron images were obtained at 2 kV accelerating voltage with no tilt on the specimen stage.

Electrochemical Impedance Spectroscopy

Electrochemical impedance spectroscopy (EIS) was done with a Princeton Applied Research (PAR) Model 273 potentiostat and a 5210 lock-in amplifier, and was controlled using PAR Model 398 software. Experiments were done in two parts: single sine wave measurements from 100 kHz to 5 Hz, and multisine measurements from 5 down to 0.05 Hz. One cm^2 of the coated panel was used as the working electrode, and excitation voltages were applied against open circuit potentials versus Ag/AgCl reference. Equivalent circuit modeling was done using Boukamp's linear least squares program Equivcrt[36] using a simple coatings model with pore resistance and coating capacitance calculated from EIS spectra.[37]

Prohesion Cabinet Exposures

Coated specimens were exposed in a mebon Prohesion cabinet for 500 hr as described elsewhere.[38,39] The exposure was performed according to ASTM G85 with the following modifications. A cyclic salt fog/dry cycle was established with one hour fog at ambient temperature and one hour dry-off at 35°C. The salt solution consisted of 0.05% sodium chloride and 0.35% ammonium sulfate by weight. Upon removal, the specimens were visually inspected and ranked according to the degree of corrosion and coating defects.

RESULTS AND DISCUSSION

In Part I of this section, the quality of images obtained by atomic force and electron microscopies is evaluated. A gold colloid standard was employed to screen AFM tips as well as measure the tip radii. Quantitative analyses of the coating surface features were performed, and measurements were cor-

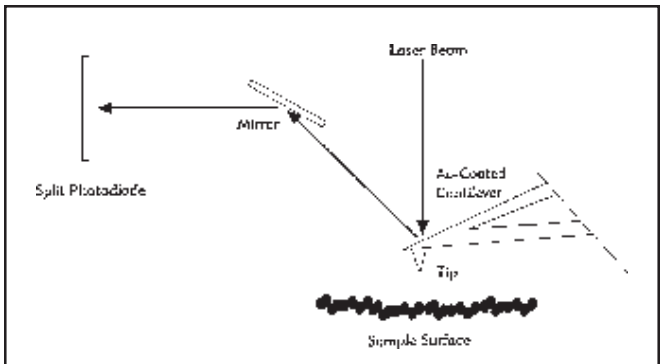

Figure 3—Schematic of AFM mechanism.

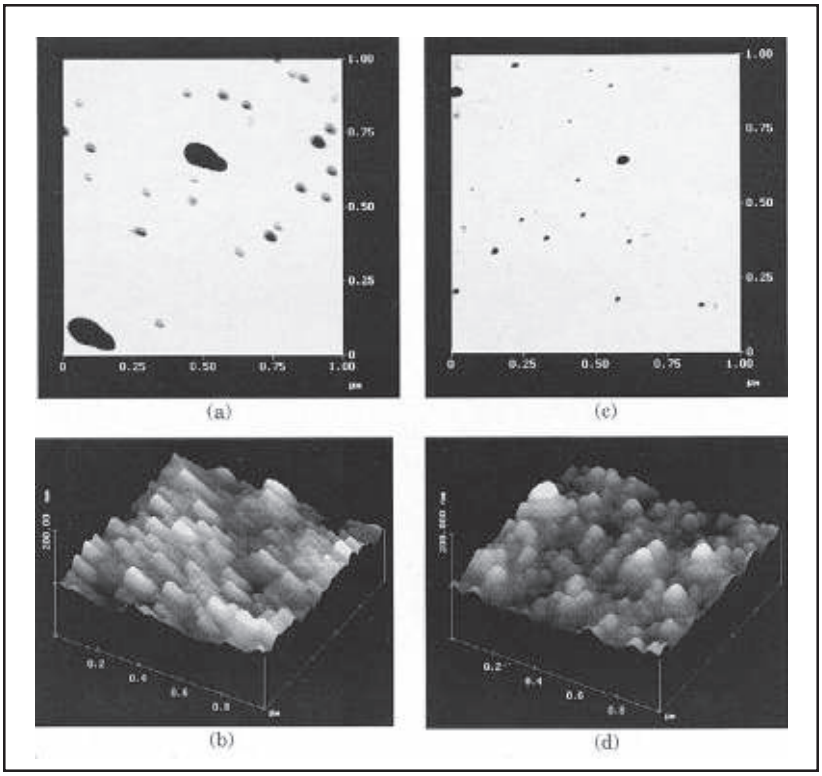

Figure 4—(a) TMAFM image of gold colloid dispersion imaged with a defective tip, (b) TMAFM image of coating I imaged with the same defective tip, (c) TMAFM image of gold dispersion imaged with a "good" tip, and (d) TMAFM image of coating I imaged with the same "good" tip.

rected for AFM tip size. Because the polymers in this study were soft, it was expected that tapping mode atomic force microscopy (TMAFM) would be more appropriate than contact mode atomic force microscopy (CMAFM) due to the lower friction forces associated with TMAFM. Both methods were used to image a subset of coatings to verify that TMAFM should be the main technique employed in this study. Scanning electron microscopy (SEM) images of the same coatings were obtained, and the complementary aspects of SEM and probe microscopies are discussed. The reader should note that the AFM images scale in microns in the xy plane but scale in nanometers in the z plane; that is, the vertical features are significantly enhanced.

In Part II of this section, characterization of particle coalescence in the applied coatings is presented. The quantitative information obtained from AFM was incorporated into a quadratic least squares fit on a three-phase composition graph so that the degree of particle coalescence for any formulation could be predicted. The results were compared to results from other coating characterization techniques, including electrochemical impedance and prohesion exposure tests.

PART I: Evaluation of Imaging Methods

***In Situ* Calibration Standard for AFM Tip Characterization:** The AFM tips used have apex radii of 20-30 nm (at a height of 5 nm), which is similar to the size range of the latex particles, 40-60 nm. Due to this size similarity, knowledge of the AFM tip morphology was required for reasons discussed in the Introduction Section. Gold colloids bound to a mica surface using a layer of 1-lysine were used as a standard to estimate the tip shape and size. The information obtained from imaging the gold standard was necessary to avoid image distortion from defective tips and to correct for AFM tip size on measurements of latex particles.

Application of Calibration Standard to Screen for Image Distortion: *Figure* 4 demonstrates the use of the gold standards to screen AFM tips. AFM images of the gold spheres and coating I that are shown in *Figures* 4a and 4b, respectively, were obtained with the same defective tip. The gold colloids (see *Figure* 4a) appeared distorted, which indicated that the tip was defective and that the data in *Figure* 4b were not representative of the surface morphology. The SEM micrograph of this tip is shown in *Figure* 5a and confirms that the tip was defective. The defective tip was replaced with a tip similar to the one shown in the SEM micrograph in *Figure* 5b. *Figure* 4c shows that the AFM image of the gold colloids obtained using the replacement tip appeared spherical, which indicated that the tip was not defective and could be used to image the coating morphology. The AFM image of coating I that was obtained with this "good" tip is shown in *Figure* 4d. The coating exhibited spherical protrusions, which we assume to be uncoalesced particles. These protrusions appeared as elongated, aligned features in the images obtained with the defective tip (see *Figure* 4b). Without the gold colloid standard, the AFM operator would not have known that the tip was defective and would have presumed that the image in *Figure* 4b was representative of the true coating morphology. This series of images demonstrates that the gold standard was an effective and necessary tool to screen AFM tips for defects.

Application of Calibration Standard to Estimate Tip Size: The average particle width in coating I measured by AFM in *Figure* 4d was 70 nm; whereas, the average particle width measured by SEM was 40 nm (image not shown). The difference in the particle widths imaged by AFM and SEM demonstrated that the AFM tip size was superimposed on the coating morphology. Characterization of the AFM tip size by the gold standard and the method of analysis applied to account for tip size on the AFM images is described in this section.

Figure 6a shows a schematic of an AFM tip that has a finite sharpness (cone angle, θ, of 20°) and size (apex radius, R_1, of 30 nm). The tip is scanning, from left to right, across a 50 nm diameter sphere. The resultant trace is shown in the following schematic. The tip edge first contacts the particle between points [a] and [c]. This first point of contact depends on the tip sharpness; for an infinitely sharp tip, the point of contact would be at a height of $^1/_2$D, and point [a] and would approach point [c] as the tip cone angle, θ, widens. The first contact between the tip and the sphere in the schematic is at point [b]. As the tip scans across the sphere, the measured distance

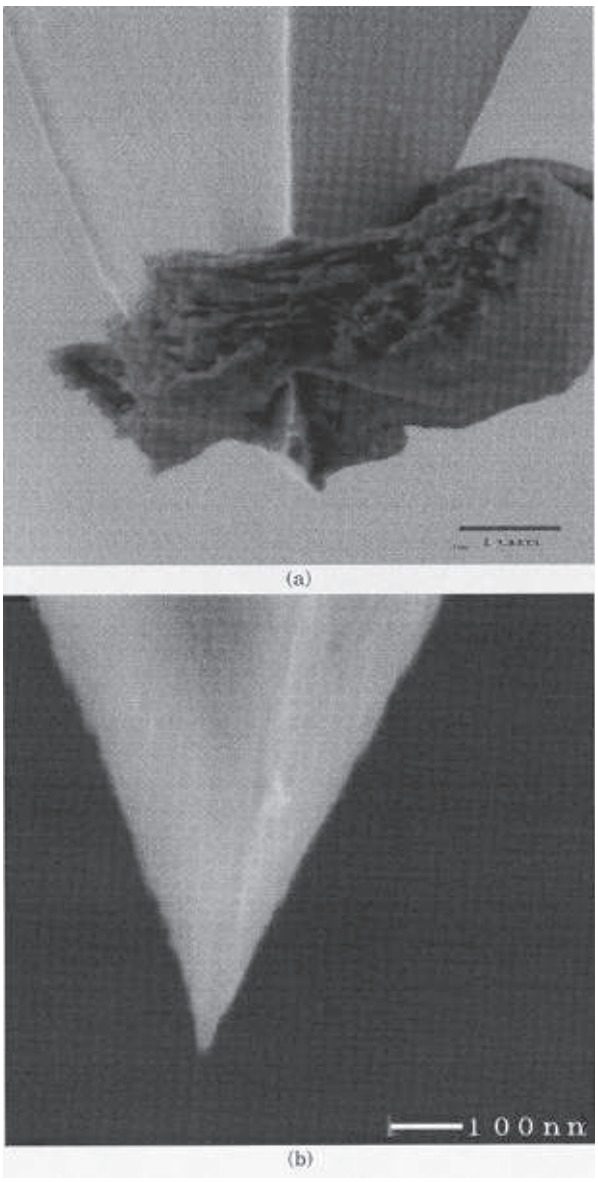

Figure 5—SEM micrographs of: (a) defective tip, and (b) defect-free tip.

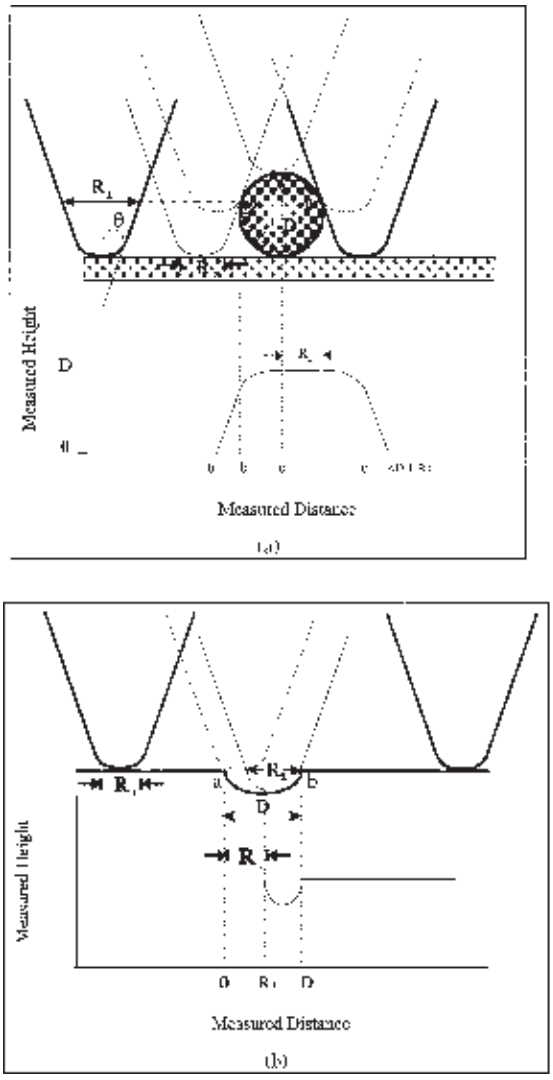

Figure 6—Schematic of tip scan and resultant trace across: (a) a sphere, and (b) a recess.

would follow the tip edge morphology until the tip apex reaches point [b]. The distance traversed by the scanner during this deflection is equal to half the tip radius at the point of first contact, R_2, less half the radius of the tip apex, R_1, such that

$$b = \frac{R_2}{2} - \frac{R_1}{2} \tag{1}$$

The sphere morphology is then imaged until the right edge of the tip apex contacts point [c], and the measured distance is

$$c = b + \frac{<D}{2} \tag{2}$$

where <D is some distance less than the sphere diameter and depends on the tip cone angle and position of the first point of contact. The tip sharpness, and thus the magnitude of <D, is not always known. For a tip with a cone angle of 20°, <D is 97% of the full diameter, D; therefore, for this analysis <D was approximated as D. At point [c], the sphere then images the tip for a distance of R_1. The sphere morphology is again imaged between points [c] and [d], such that the distance traversed when the tip reaches point [d] is

$$d = c + R_1 + \frac{D}{2} \tag{3}$$

After the tip apex reaches point [d], the tip left edge morphology is imaged until the tip touches the substrate. The total distance measured, D_m, is

$$D_m = d + \frac{R_2}{2} - \frac{R_1}{2} \tag{4}$$

Combining equations (1) through (4) yields:

$$D_m = R_2 + D \tag{5}$$

Thus, the protruding features would appear wider by R_2, which varies with feature height. The measured height, however, is accurate and equal to the particle diameter. The set of R_2 values were measured at 8, 14, and 29 nm diameter gold spheres. The estimated R_2 was then subtracted from the measured diameter of the coating features.

Figure 6b shows a resultant trace obtained from the superposition of a TMAFM tip scanning a hemispherical recessed region. As the tip apex reaches the recess corner, point [a], it would hang above the recess until the left edge of the tip also crossed point [a]. Consequently, the scanner would have traversed across the recess for a distance R_1, but no change in morphology would have been detected. Upon descent of the tip into the recess, the corner, at point [a], would trace the tip left edge morphology. When the tip edge clears the recess side wall, the tip would trace the inner morphology of the recessed region until the right edge of the tip contacts the right recess corner, point [b]. This corner would then trace the morphology of the right tip edge. The resulting trace would show a recessed feature with a measured diameter,

$$D_m = D - R_1 \quad (6)$$

and the side walls that have the morphology of the tip edges. In short, the recessed feature would appear more narrow than the actual diameter, and the measured depth would be accurate if the tip could penetrate to the bottom of the feature, i.e., if R_2 is less than D.

The value of R_2 measured for the 8 nm gold colloid was used to represent the tip apex radius, R_1. The diameters of the recessed features imaged in the polymer coatings were corrected for the tip apex radius. The feature sizes discussed in the remainder of this paper have been corrected for tip size.

Comparison of Imaging Methods: Contact and tapping mode AFM, as well as SEM, were used to image a subset of coatings. SEM and AFM showed similar qualitative results, but the SEM resolution and contrast was very poor. Quantitative, three-dimensional information was not available from SEM images and the lateral features sizes of these coatings were near the 20 nm resolution limit of SEM in bulk materi-

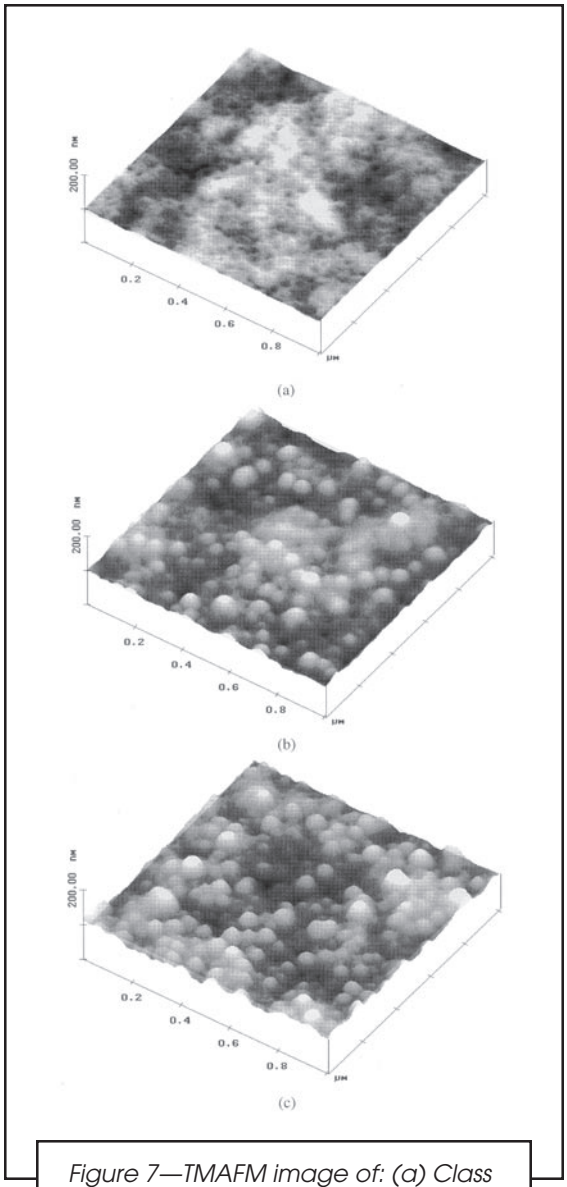

Figure 7—TMAFM image of: (a) Class I Coating 620, (b) Class II Coating N, and (c) Class III Coating 630.

Table 2—Classification and Ranking for 14 Blended Hybrid Coatings

Sample ID	Recessed Features Diameter/Depth	Particle Size		# Density (#/μm²)
		Width	Height	
Class I Coatings				
620 (C)	70 nm/2 nm	none	none	none
B	60 nm/2-5 nm	30 nm	10 nm	15
H	80 nm/2-5 nm	35-40 nm	15 nm	25
Class II Coatings				
610 (A)	few	20-40 nm	5-10 nm	27
D	70 nm/3 nm	25-70 nm	5-20 nm	35
J	70 nm/3 nm	25-70 nm	5-20 nm	40
G	few	30-40 nm	10-20 nm	50
N	75 nm/3 nm	25-70 nm	5-20 nm	50
K	70 nm/3 nm	20-70 nm	5-20 nm	60
Class III Coatings				
F	few	10-60 nm	5-20 nm	60
L	few	40 nm	10 nm	60
I	few	40, 70 nm	15 nm	80
M	45 nm/3 nm	50 nm	15-20 nm	80
630 (E)	few	30, 15 nm	15, 10 nm	85

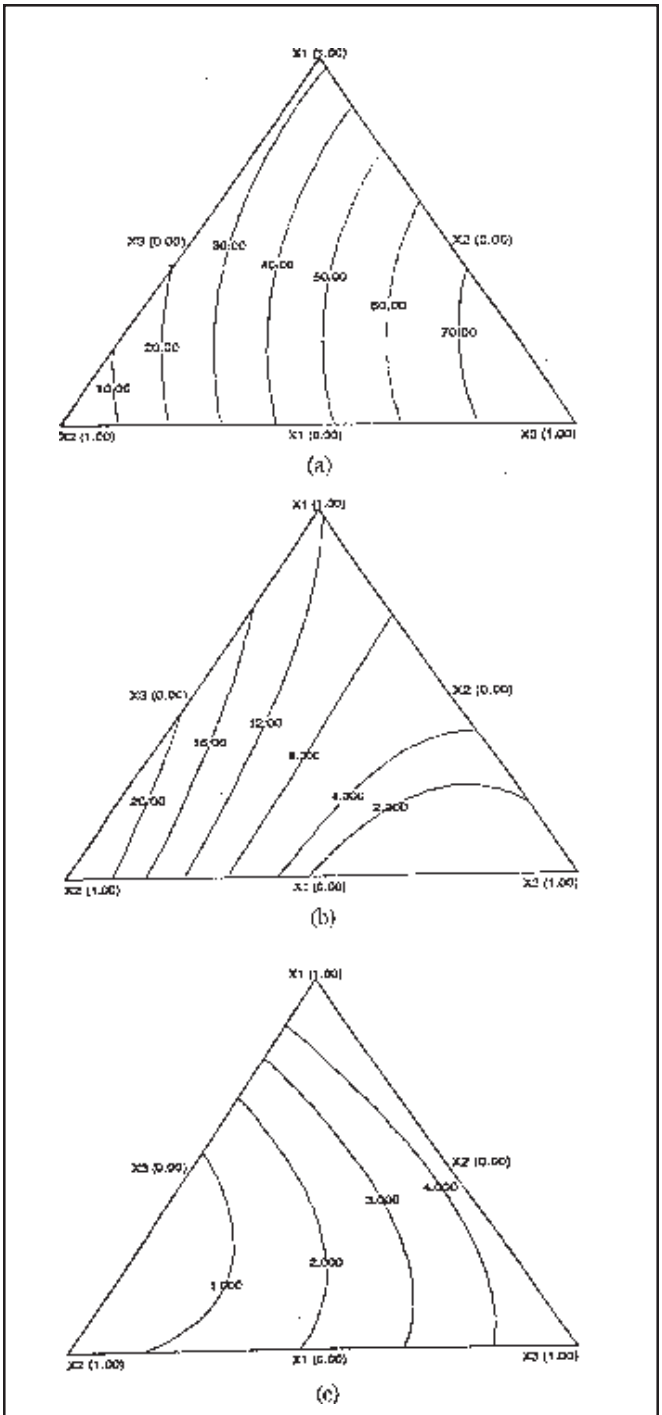

Figure 8—Quadratic regression analysis on a three-component composition chart of: (a) particle density, (b) pore resistance, and (c) corrosion spot density, where X_1=Flexthane 610, X_2=Flexthane 620, and X_3=Flexthane 630.

als. The contrast in the SEM images of these small particle size latex films was poor. Although the surfaces were coated with a thin layer of platinum (1 nm), the secondary electron yield was dependent on the bulk material. Because the polymeric materials do not provide good secondary electron yields, the signal to noise ratio is lower than would be expected for a conductive material. Another problem associated with SEM imaging of coatings was that the material was beam sensitive; heat generated from the penetrating electrons would melt or vaporize the polymer. Consequently, there was a low maximum time and beam intensity that could be applied to image an undamaged surface. These limits further decreased the resolution.

CMAFM, in general, provided acceptable results, but the friction forces caused image streaking. As well, SEM of used CMAFM tips showed that the tips were frequently contaminated with the polymer and/or other debris. TMAFM provided clear, reproducible images of the coating morphology and was defined as the most appropriate and more accurate technique for imaging these polymer samples.

PART II: Evaluation of Polymer Film Formation

Characterization of Particle Coalescence: A series of 14 waterborne latex coating blends was studied in order to characterize polymer coalescence as a function of composition. The coatings were developed by blending three acrylic-polyurethane hybrid polymer dispersions, Flexthane 610, 620, and 630. *Table* 1 in the Experimental Section lists the coating labels with their corresponding compositions and *Figure* 2 shows the position of each blend on a three-phase composition diagram.

Tapping mode atomic force microscopy (TMAFM) was chosen as the main imaging technique used in this study for reasons previously discussed. Particles were defined as features that protruded above the average surface plane and had a diameter (after correction for the tip radius) of 20-60 nm, consistent with the particle size distribution of 40-60 nm measured by light scattering methods. The average particle size distribution for each dried coating was approximated by measuring the size of the particles (with the cross-section analysis software) and correcting for tip radius. The number of particles that protruded at least 8 nm above the average surface plane was counted to yield a number density of particles within the film. This count was manually performed on images with a contour color scheme set such that features protruding more than 8 nm were white, while the remaining surface was black.

In *Table* 2, the coatings are ranked according to the degree of particle coalescence as determined by particle size distribution and particle number density. Qualitative and quantitative examination of the TMAFM images and degree of particle coalescence led to classification of the coatings into three types of films. *Figure* 7 presents the images of one coating representative of each class listed in *Table* 2. *Figure* 7a shows coating Flexthane 620, which was classified in Class I. Class I films were smooth with few detectable individual particles. These coatings had an ordered array of recessed features that were 70 nm in diameter and 2-3 nm deep. The protruding features seen in these coatings were relatively small, 30-35 nm wide. These coatings were considered the best film formers. *Figure* 7b shows coating N, which was representative of films in Class II. Class II films exhibited the coalescence of particles into large clumps with few discrete (20-60 nm) features. Some of these coatings exhibited recessed features and there were a wide range of protrusions observed (20-70 nm). Class II coatings were considered fair film formers. *Figure* 7c shows an image of coating 630, which was representative of

films in Class III. Class III films showed numerous distinct particles. These films showed no ordered array of recessed features and were considered to be poor film formers. It is noted that coatings in Class I and II contained higher concentrations of 620 and/or 610; whereas, coatings in Class III were high in 630.

Figure 8a shows the results from a quadratic regression analysis of the particle density data (see *Table* 1) as a function of composition. The contours show that 620 provided the best coalesced films while 630 produced the least coalesced films. This trend was not surprising since, as discussed in the Introduction Section, the T_g of 620 is relatively low, while that of 630 is relatively high. Quantitative information from the AFM data that can be used in such contour plots will facilitate the ability to predict the film formation characteristics of other mixtures.

Comparison of AFM Results with Other Characterization Methods: To further substantiate the ability of AFM to explicitly determine the film formation characteristics of coatings, EIS and Prohesion cabinet exposures were performed on metal specimens coated with the same hybrid materials. These evaluations were performed because improved film formation should produce improved barrier properties. Poor film formation should lead to poorly coalesced regions within the coating, such as pinholes and/or cracks, which cause the substrate to be more susceptible to a corrosive environment. EIS yields a coating pore resistance, which reflects the ability of a coating to protect the substrate from a corrosive electrolyte. *Figure* 8b shows the results from a quadratic regression analysis of the pore resistance values of the specimens immersed in 1M NaCl solution. The contour plot of the EIS data clearly displays a dramatic increase in pore resistance as the 630 concentration decreases, especially in the direction of increasing 620. This result reflects an increased resistance to penetration of electrolyte ions and reflects good film formation. Prohesion cabinet exposures directly ascertain corrosion protection of the substrate provided by the coatings, and the results are quantified by a count of localized corrosion spots per a unit area. *Figure* 8c shows the results from a quadratic regression analysis of the corrosion spot density. Consistent with EIS results, these data show that corrosion protection improves with decreasing 630 and increasing 620 concentrations. The AFM results suggest that increasing 610 and 620 concentrations in the hybrid coatings improved film formation, which, in turn, as shown by the EIS and Prohesion test, improved the barrier properties of the coatings.

It should be noted that certain mixtures of these dispersions have displayed synergistic effects in hardness and adhesion. For example, when comparing coatings without additional coalescing solvents, a 17:17:66 blend of 610:620:630 has a higher pendulum (ASTM D 4366) and pencil (ASTM D 3363) hardness than 630, while still having the G.E. impact strength (ASTM D 2794) as 610 and 620. This seems to be additional evidence that the blending of the harder 630 with 610 and 620 aids significantly in film formation without additional coalescing aids or heat. It is important to note that these benefits can be obtained at a minimum volatile organic component (VOC) level (<150 g/L).

Other Observations: One notable observation from the AFM images obtained in this study was the presence of recessed areas in the surface morphologies (see AFM images of coatings in Class I). Similar recessed features have been rarely reported. Vanderhoff[3] performed SEM analysis on replicas of coatings from a poly(styrene-butadiene) copolymer latex dispersion and observed a number of "extracted" particles. He noted that the number of extracted particles decreased with increased film coalescence; and, therefore, attributed the phenomenon to removal of uncoalesced particles during the replica sample preparation. More recently, Juhué et al.[18,19] used AFM to study film formation from poly(butyl methacrylate) latex dispersions. Their studies focused on the effect of surfactants on the face-centered cubic packing structure of the particles and particle coalescence at various stages of annealing. They observed deformations that were smaller than the particle diameters and the spherical nature of the particles were evident at each stage of coalescence. It should be noted that the particle size in these previous studies was 250-500 nm, which is substantially larger and easier to analyze than the 40-60 nm particle size in this work. We have observed similar features on a coating containing Flexthane 620 and titanium dioxide pigment.

The recessed features observed in this work were prominent in the smoothest films and were not evident on the films with high particle densities. These features are not clearly visible by SEM, as discussed in Part I, and it is likely that they have not been previously observed since AFM has not been widely applied in such applications. The recessed features in the hybrid coatings were 2-3 nm in depth and their diameter was approximately 70 nm. A solvent-based coating and four other aqueous dispersion coatings were analyzed by AFM and compared to the hybrid coatings in this study. The solvent-based coating, as expected, exhibited molecular-level smoothness (<5 nm roughness). There were no recessed or protruding features observed in this coating. In fact, this surface appeared substantially smoother than 620 (coating C), which was the best hybrid film former. The four latex-based coatings showed both smooth and rough morphologies, but none exhibited the network of recessed features. However, these films were in storage for several months and it is well-known that coalescence can continue over a period of months. The films studied in this work were allowed to film form for less than one month. A study of film formation with time will be performed using AFM.

The source of the ordered network of recessed features is unknown; future studies in this area could lend new insight into the film formation mechanism of latex-based coatings.

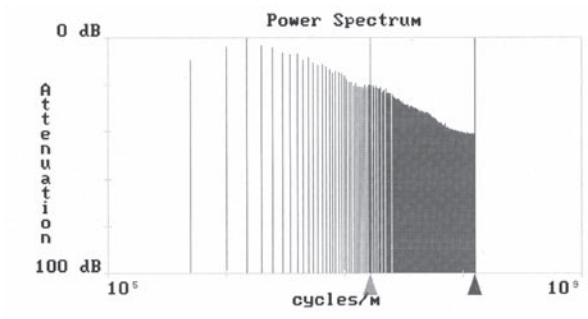

Figure 9—Power spectral density plot of Flexthane 620. The peak indicates the spacing of the ordered network of recessed features.

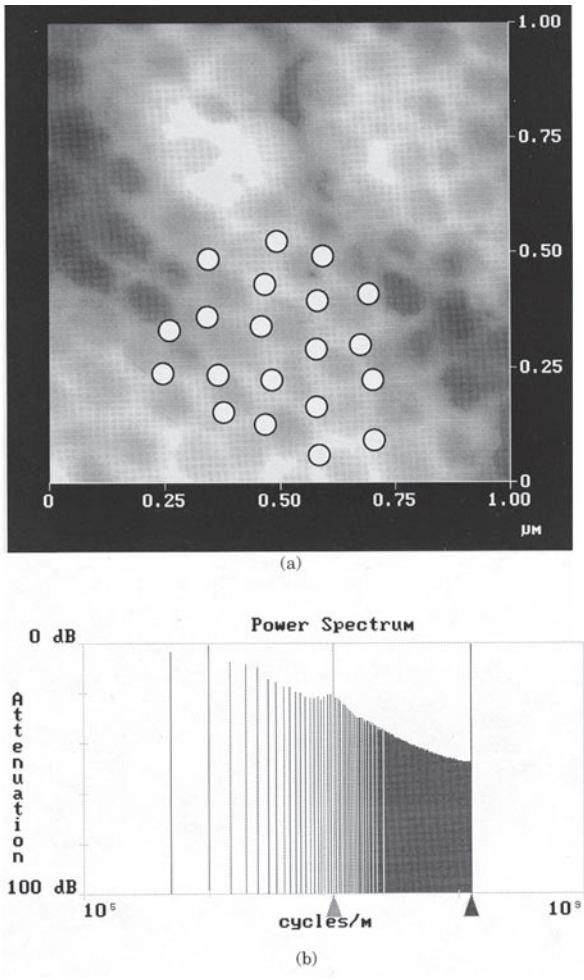

Figure 10—(a) Topview AFM image of a Flexthane coating that exhibits a highly ordered array of recessed features; (b) Power spectral density plot of AFM image shown in (a).

Figure 9 is a power spectral density plot generated from an AFM image of 620. It is seen that a peak occurs in this plot at a wavelength of 60 nm, which corresponds to the diameter of the recessed features. The distinct peak is clear evidence that the recessed features form an ordered network. Because the features are ordered, it is plausible that their formation is related to the packing arrangement of the particles during the drying process. The particles have sufficient time during the drying process to pack in the most thermodynamically favored arrangement, i.e., close packed. As the solvent evaporates, the particles come closer and begin to coalesce; and as the particles dry, they also begin to shrink. A sequence of events where the particles pack, coalesce, then shrink would result in the coalesced network observed in the AFM images. For example, *Figure* 10a shows a topview AFM image of a hybrid coating being investigated in a parallel study. This film was very level and exhibited a clear hexagonal arrangement of recessed features. The circles superimposed on this image illustrate the original face centered cubic particle packing that could lead to the coalesced network imaged by AFM. *Figure* 10b is the power spectral density plot for this same image and a peak is observed at 100 nm, which when corrected for an apex tip size of approximately 15 nm indicates that the recessed features are 115 nm in diameter. The number average particle size in this emulsion was 64 nm. The fact that the recessed regions are nearly a factor of two larger than the original particle size supports the idea that the polymer shrinks significantly upon drying. If this proposed mechanism is valid, the recessed feature size should depend on the packing arrangement, the particle size, the extent of particle swelling in the dispersion, and the rate of drying versus coalescence.

CONCLUSIONS

This work had demonstrated that AFM is an excellent tool for assessing film formation. Techniques, such as SEM, that have conventionally been used for similar studies cannot provide the vertical resolution or quantitative information available from AFM. Although artifacts are imposed on the results by the AFM tip, a gold colloid standard can be used to correct for them. With this technique we have developed a means of describing the extent of particle coalescence in the system studied. The AFM results, which were supported by other barrier characterization techniques, such as EIS and Prohesion cabinet tests, indicate the Flexthane 620 was a better film former than Flexthane 610 and, especially, Flexthane 630. By formulating hybrid blends, film formation of the Flexthane 630 was improved. The results suggest that benefits may be obtained from mixtures of the dispersions by offering a compromise between polymer hardness and film formation. A notable observation from this work was the ordered network of recessed features in the better film formers. These recesses were not observed by SEM. The clear hexagonal order evident in these networks indicates that their source was dependent on the packing structure of the coalescing particles. Further investigation of this phenomenon could provide new insight into the film formation mechanism and lead to improved methods for tailoring coating formulations to yield the desired characteristics.

ACKNOWLEDGMENTS

The authors would like to acknowledge J.R. Stets for the SEM work and L. Mercando for enlightening discussions throughout this effort.

References

(1) Dillon, W.E., Matheson, D.A., and Bradford, E.B., "Sintering of Synthetic Latex Particles," *J. Colloid Sci.*, 6, 109 (1951).
(2) Brown, G.L., "Formation of Films from Polymer Dispersions," *J. Poly. Sci.*, 22, 423 (1956).
(3) Vanderhoff, J.W., "Mechanism of Film Formation of Lattices," *Br. Poly. J.*, 2, 161 (1970).
(4) Sheetz, D.P., "Formation of Films by Drying Latex," *J. Appl. Poly. Sci.*, 9, 3759 (1965).
(5) Voyutskii, S.S. and Usinova, Z.M., "Role of Autohesion During Film Formation from Latex," *J. Adhesion*, 9, 39 (1977).
(6) Eckersley, S.T. and Rudin, A., "Mechanism of Film Formation from Polymer Latexes," JOURNAL OF COATINGS TECHNOLOGY, 62, No. 780, 39 (1990).
(7) Kendall, K. and Padget, J.C., "Contact of Polymer Latex Particles with Metals," *J. Adhesion and Adhesives*, July, 149 (1982).
(8) Sheehan, J.G., Takamura, K., Davis, H.T., and Scriven, L.E., "Microstructure Development in Particulate Coatings Examined with High-Resolution Cryogenic Scanning Electron Microscopy," *Coating Analysis, TAPPI J.*, 76, 93 (1993).

(9) Linné, M.A., Klein, A., Miller, G.A., Sperling, L.H., and Wignall, G.D., "Film Formation from Latex: Hindered Initial Interdiffusion of Constrained Polystyrene Chains Characterized by Small-Angle Neutron Scattering," *J. Macromol. Sci.-Phys.*, B27, 217 (1988).
(10) Yoo, J.N., Sperling, L.H., Glinka, C.J., and Klein, A., "Characterization of Film Formation from Polystyrene Latex Particles via SANS. 1. Moderate Molecular Weight," *Macromolecules*, 23, 3962 (1990).
(11) Yoo, J.N., Sperling, L.H., Glinka, C.J., and Klein, A., "Characterization of Film Formation from Polystyrene Latex Particles via SANS. 2. High Molecular Weight," *Macromolecules*, 24, 2868 (1991).
(12) Zhao, C-Le, Wang, Y., Hruska, Z., and Winnik, M.A., "Molecular Aspects of Latex Film Formation: An Energy-Transfer Study," *Macromolecules*, 23, 4082 (1990).
(13) Binning, G. and Quate, C.F., "Atomic Force Microscope," *Phys. Rev. Let.*, 56, 930 (1986).
(14) Alexander, S., Hellemans, L., Marti, O., Schnei, J., Elings, V., and Hansma, P.K., "An Atomic-resolution Atomic-Force Microscopy Implemented Using an Optical Lever," *J. Appl. Phys.*, 65, 164 (1988).
(15) Goss, C.A., Brumfield, J.C., Irene, E.A., and Murray, R.W., "In Situ Atomic Force Microscopic Imaging of Electrochemical Formation of a Thin Dielectric Film. Poly(Phenylene oxide)," *Langmuir*, 8, 1459 (1992).
(16) Stange, T.G., Mathew, R., and Evans, D.F., "Scanning Tunneling Microscopy and Atomic Force Microscopy Characterization of Polystyrene Spin-Coated onto Silicon Surfaces," *Langmuir*, 8, 920 (1992).
(17) Saraf, R.F., "Early-Stage Phase Separation in Polyimide Precursor Blends: An Atomic Force Microscopy Study," *Macromolecules*, 26, 3623 (1993).
(18) Juhué, D. and Lang, J., "Effect of Surfactant Postadded to Latex Dispersion on Film Formation: A Study by Atomic Force Microscopy," *Langmuir*, 9, 792 (1993).
(19) Goh, M.C., Juhué, D., Leung, O., Wang, Y., and Winnik, M.A., "Annealing Effect on the Surface Structure of Latex Films Studied by Atomic Force Microscopy," *Langmuir*, 9, 1319 (1993).
(20) Radmacher, M., Tillmann, R.W., Fritz, M., and Gaub, H.E., "From Molecules to Cells: Imaging Soft Samples with the Atomic Force Microscope," *Science*, 257, 1900 (1992).
(21) Westra, K.L., Mitchell, A.W., and Thomson, D.J., "Tip Artifacts in Atomic Force Microscope Imaging of Thin Film Surfaces," *J. Appl. Phys.*, 74, 3608 (1993).
(22) Magonov, S.N., Gorenberg, A. Ya., and Cantow, H.-J., "Atomic Force Microscopy on Polymers and Polymer Related Compounds," *Polymer Bulletin*, 28, 577 (1992).
(23) Jensen, F., "Calibration of the Atomic Force Microscope by Means of a Pyramidal Tip," *Rev. Sci. Instrum.*, 64, 2595 (1993).
(24) Montelius, L. and Tegenfeldt, J.O., "Direct Observation of the Tip Shape in Scanning Probe Microscopy," *Appl. Phys. Lett.*, 62, 2628 (1993).
(25) Barbet, J., Garvin, A., Thimonier, J., Chauvin, J., and Rocca-Serra, J., "Scanning Tunneling Microscopy of Colloid Gold Beads," *Ultramicroscopy*, 50, 355 (1993).
(26) Vesenka, J., Manne, S., Giberson, R., Marsh, T., and Henderson, E., "Colloidal Gold Particles as an Incompressible Atomic Force Microscope Imaging Standard for Assessing the Compressibility of Biomolecules," *Biophys. J.*, 65, 992 (1993).
(27) Ohmi, T. and Aoyama, S., "Calibration of Height in Atomic Force Microscope Images with Subnanometer Scale Silicon Dioxide Steps," *Appl. Phys. Lett.*, 61, 2479 (1992).
(28) Sheiko, S.S., Moller, M., Reuvekamp, E.M.C.M., and Zandbergen, H.W., "Calibration and Evaluation of Scanning-Force-Microscopy Probes," *Phys. Rev. B*, 48, 5675 (1993).
(29) Thundat, T., Zheng, S-Y., Chen, G.Y., Sharp, S.L., and Warmack, R.J., "Characterization of Atomic Force Microscope Tips by Adhesion Force Measurements," *Appl. Phys. Lett.*, 63, 2150 (1993).
(30) Hutter, J.L. and Bechhoefer, J., "Calibration of Atomic-Force Microscope Tips," *Rev. Sci. Instrum.*, 64, 1868 (1993).
(31) Burnham, N.A., "Apparent and True Feature Heights in Force Microscopy," *Appl. Phys. Lett.*, 63, 114 (1993).
(32) U.S. Patent 5,173,526 "Aqueous Polyurethane-Vinyl Polymer Dispersions for Coatings Applications."
(33) Hegedus, C.R. and Kloiber, K.A., "Acrylic-Polyurethane Aqueous Dispersions: Structure and Properties in Industrial Coatings," *Proc. 21st Waterborne, Higher-Solids & Powder Coatings Symp.*, New Orleans, LA, February 9-11, 1994.
(34) Gorman, J.W. and Hinman, J.E., *Technometrics*, 4(3), 463 (1962).
(35) McLean, R.A. and Anderson, V.L., *Technometrics*, 8(3), 447 (1966).
(36) Boukamp, B.A., *Solid State Ionics*, 20, p. 31 (1986).
(37) Skerry, B.S., Alavi, A., and Lindgren, K.I., "Environmental and Electrochemical Test Methods for the Evaluation of Protective Organic Coatings," JOURNAL OF COATINGS TECHNOLOGY, 60, No. 765, 97 (1988).
(38) Cremer, N.D., "Prohesion Compared to Salt Spray and Outdoors Cyclic Methods of Accelerated Corrosion Testing," Presented at the Federation of Societies for Coatings Technology Annual Meeting, October 1989, New Orleans, LA.
(39) Simpson, C.H., Ray, C.J., and Skerry, B.S., "Accelerated Corrosion Testing Using a Cyclic Corrosion Weathering Method," *J. Protective Coat. Linings*, 8(5), 28 (1991).